



In-situ TEM observation of structural changes in nano-crystalline CoCrCuFeNi multicomponent high-entropy alloy (HEA) under fast electron irradiation by high voltage electron microscopy (HVEM)

Takeshi Nagase ^{a, b, *}, Philip D. Rack ^{c, d}, Joo Hyon Noh ^d, Takeshi Egami ^{c, d, e}

^a Research Center for Ultra-High Voltage Electron Microscopy, Osaka University, 7-1, Mihogaoka, Ibaraki, Osaka 567-0047, Japan

^b Division of Materials and Manufacturing Science, Graduate School of Engineering, Osaka University, 2-1, Yamada-Oka, Suita, Osaka 565-0871, Japan

^c Oak Ridge National Laboratory, P.O. Box 2008, Oak Ridge, TN 37831, USA

^d Department of Materials Science and Engineering, University of Tennessee, Knoxville, TN 37996, USA

^e Department of Physics and Astronomy, University of Tennessee, Knoxville, TN 37996, USA

ARTICLE INFO

Article history:

Received 12 July 2014

Received in revised form

8 December 2014

Accepted 11 December 2014

Available online 2 January 2015

Keywords:

A. High-entropy alloys

B. Irradiation effects

B. In situ

D. Microstructure

ABSTRACT

The structural changes induced in a CoCrCuFeNi multicomponent nano-crystalline high-entropy alloy (HEA) under fast electron irradiation were investigated by *in-situ* transmission electron microscopy (TEM) using a high voltage electron microscope (HVEM). A fine-grained face centered cubic (*fcc*) single phase was obtained in the sputtered specimens. The *fcc* solid solution showed high phase stability against irradiation over a wide temperature range from 298 to 773 K, and remained as the main constituent phase even when the samples were irradiated up to 40 displacement per atom (dpa). Moreover, the irradiation did not seem to induce grain coarsening. This is the first report on the irradiation damage in 5-component HEA under MeV electron irradiation.

© 2014 Elsevier Ltd. All rights reserved.

1. Introduction

In view of maintaining sustainable energy supply and ensuring the safe operation of nuclear reactors, the development of new and advanced nuclear materials is in high demand. Many studies have been conducted on nuclear materials to understand their degradation under irradiation to determine their optimal operating conditions and to evaluate their lifetimes. However, there is very little scope for improving various currently existing nuclear materials because they have been fully matured in technology. Therefore, a new generation of structural materials with superior resistance to irradiation damage is much sought after to satisfy the future need for safer and more efficient nuclear systems.

Recently, a new generation of structural materials, termed as multicomponent high-entropy alloys (HEAs), has been developing [1–4]. This class of alloys consists of multicomponent elements with an approximately equiatomic ratio of various components for

maximizing the compositional entropy, which stabilizes the solid solution phase. Mixing of various elements results typically in high atomic-level stress, which leads to the possibility of achieving high irradiation resistances through unique damage healing mechanisms [5]. A multicomponent ZrHfNb alloy with an approximately equiatomic ratio of its constituent elements is reported to show high phase stability against fast electron irradiation [6,7]. Thus HEAs have remarkable potential to possess superior phase stability against irradiation damage; however, to the best of our knowledge there are hardly any systematic studies reported on the phase stability of multicomponent solid solutions in HEAs against irradiation damage; in particular, there is no experimental report about the irradiation damage in HEAs under MeV electron irradiation. This paper is the first report of *in-situ* TEM observation of the phase stability of HEA against the irradiation damage introduced by fast electron.

2. Experimental

A CoCrCuFeNi five-component alloy was deposited onto a NaCl [001] substrate using an AJA International ATC 2400-V system using an alloy target made of up equiatomic concentrations of elemental

* Corresponding author. Research Center for Ultra-High Voltage Electron Microscopy, Osaka University, 7-1, Mihogaoka, Ibaraki, Osaka 567-0047, Japan. Tel.: +81 6 6879 7941; fax: +81 6 6879 7942.

E-mail address: t-nagase@uhvem.osaka-u.ac.jp (T. Nagase).

Co, Cu, Cr, Fe, and Ni targets [8]. The target power was 200 W, processing pressure was 5 mTorr Ar, and the measured deposition rate was ~ 4.8 nm/min. The samples with thicknesses (25 nm, 100 nm and 1 μ m) samples were made by linearly adjusting the time appropriately to 5.2, 20.8 and 208.3 min. The CoCrCuFeNi thin film on NaCl substrate was then made to float on distilled water and mounted on a grid for transmission electron microscopy (TEM) analysis and for irradiation experiments by HVEM.

Conventional TEM and high resolution electron microscopy (HREM) observations were carried out for investigating the microstructure of sputtered specimens using a Hitachi H-800 TEM microscope equipped with an energy dispersive spectrometer (EDS) at an acceleration voltage of 200 kV and a JEOL JEM-ARM200F/UHR electron microscope operated at 200 kV, respectively. Structural change of the sputtered HEAs induced by thermal annealing and fast electron irradiation was investigated by *in-situ* TEM using an ultra-high voltage H-3000 electron microscope (HVEM). Electron irradiation was carried out using an ultra-high voltage H-3000 electron microscope (UHVEM). The dose rate was evaluated by using the Faraday cup in the UHVEM. The applied electron dose rate was fixed at $5.7 \times 10^{24} \text{ m}^{-2} \text{ s}^{-1}$. The irradiation was carried out at 298 K (room temperature) and 773 K under a vacuum of approximately 8.0×10^{-6} Pa. On the basis of the model of the local temperature rise in a specimen irradiated by an electron beam proposed by Kiritani et al., the temperature increase resulting from electron irradiation was found to be negligible in the present study because of the high thermal conductivity of metallic materials [9]. The microstructural changes caused by electron irradiation were observed by *in-situ* TEM observations using the UHVEM at 2.0 MV. Bright-field (BF) images and selected area diffraction (SAD) patterns were captured by using imaging plates. The electron irradiation was interrupted to acquire images. The effect of the additional electron irradiation during the *in-situ* TEM observation was negligible owing to the low dose rate.

The collision cross section for atomic displacement (σ) of the CoCrCuFeNi specimen was estimated according to the linear mixture rule for pure elements, and the σ for pure elements was calculated using the McKinley–Feshbach formula [10–12]. In the present study, the threshold energy (E_d) for the atomic

displacement of Co, Cr, Cu, Fe, Ni, and Al atoms was evaluated at 22, 24, 19, 20, 24, and 14 eV, respectively. The data for Co, Cr, Cu, Fe, Ni, and Al were obtained from the experimental data [13,14] and that for Cr was estimated from the melting temperature [15,16]. In addition, σ_{Al} was also calculated in the present study because the previous reports on the formation of solid solution phase in AlCoCrCu_{0.25}FeNi (body centered cubic, bcc) [4] and Al_{0.5}CoCrFeNi (face centered cubic, fcc) [4]. Fig. 1 shows the σ of pure Co, Cr, Cu, Fe, Ni, and Al. By fast electron irradiation at 2.0 MeV, the σ was roughly estimated as 79 barns for CoCrCuFeNi (Co₂₀Cr₂₀Cu₂₀Fe₂₀Ni₂₀, at.%) alloy. This value corresponds to 0.045 dpa/s at the dose rate of $5.7 \times 10^{24} \text{ m}^{-2} \text{ s}^{-1}$.

3. Results

3.1. Sample characterization

Fig. 2 shows the TEM-BF images (a) and (b), TEM-SAD patterns (a') (b') (a''), and TEM-dark field (DF) images (b''), in addition to the HVEM-BF image (c) and HVEM-SAD patterns (c') (c'') of the sputtered CoCrCuFeNi alloy specimens. The BF image (a) of the 25 nm thick specimen shows nanocrystalline contrast and the SAD pattern (a') shows Debye rings. This indicates the formation of nanocrystalline structures. The formation of a nanocrystalline structure in the 100 nm thick specimen can be confirmed by the nanocrystalline contrast in the BF image (b) and DF image (b'') and by the Debye rings in the SAD pattern (b'). The HVEM-BF image (c) of the 1 μ m thick specimen showed a fine crystalline contrast with grain sizes significantly larger than those present in the 25 nm and 100 nm thick specimens. The Debye rings can also be seen in the HVEM-SAD pattern (c'), which indicates that the position of each Debye ring shown by the 1 μ m thick specimens is identical to that shown by the 25 nm and 100 nm thick specimens. Fig. 2(a'') and (c'') show the results of the analysis of the SAD patterns of the 25 nm and 1 μ m thick specimens. The constituent phase of both specimens can be identified as the disordered fcc solid solution phase and the constituent phases were independent of the sample thickness. Fig. 3(a) shows the HREM image of the 25 nm thick specimen. Nanocrystalline grains with sizes less than 10 nm could be observed. The central nanocrystal indicated by the white arrow can be identified as the fcc solid solution by the fast Fourier transform (FFT) pattern (Fig. 3(a')). Table 1 summarizes the characteristics of the sputtered CoCrCuFeNi alloys. The average (Table 1(a)) and standard deviation (Table 1(b)) of the alloy composition were obtained by the analysis of 15 different positions in the same specimen. We could not detect any microscale fluctuations of composition in the sputtered specimen, as shown in Table 1(b). Table 1(a) shows the following tendencies: (1) the Cu ratio in the alloys may be slightly higher than the ratio of the other constituent elements in the CoCrCuFeNi alloys, regardless of the specimen thickness and (2) the composition of all the elements (x) is within $17 \leq x \leq 27$ in specimens with thicknesses of 25 nm, 100 nm, and 1 μ m. These results indicate the formation of five-component CoCrCuFeNi alloys with approximately the same composition in the sputtered specimens. It was reported that three parameters including ΔH_{mix} , ΔS_{mix} , and delta parameter were important for the formation of a solid solution phase in multicomponent alloys [5]. The values of these parameters are shown in Table 1(c). The three parameters of CoCrCuFeNi alloys are similar to the values previously reported for HEAs with a single solid solution structure, such as AlCoCrCu_{0.25}FeNi (bcc), Al_{0.5}CoCrFeNi (fcc), CoCuFeNiV (fcc), etc. [4]. A low delta value, a high ΔS_{mix} value, and a small positive ΔH_{mix} value indicate that the nanocrystalline CoCrCuFeNi specimen under consideration in

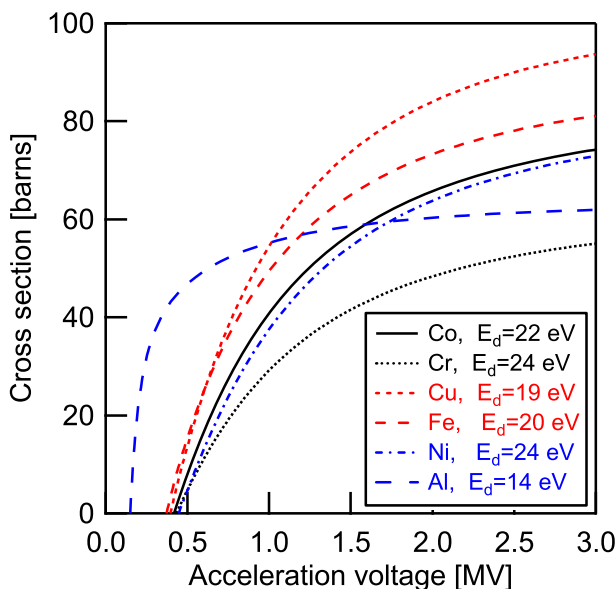


Fig. 1. The cross section of the atomic displacements of the pure elements calculated using the McKinley–Feshbach formula.

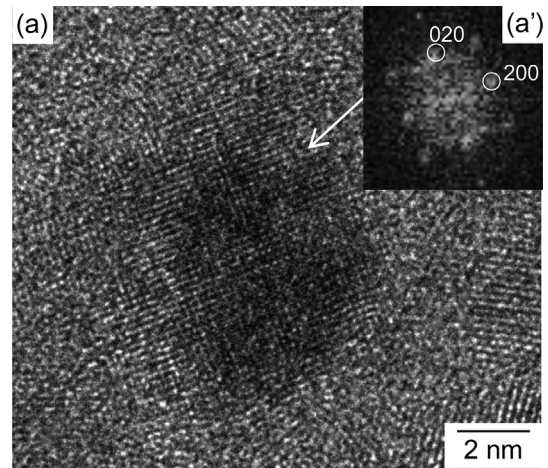
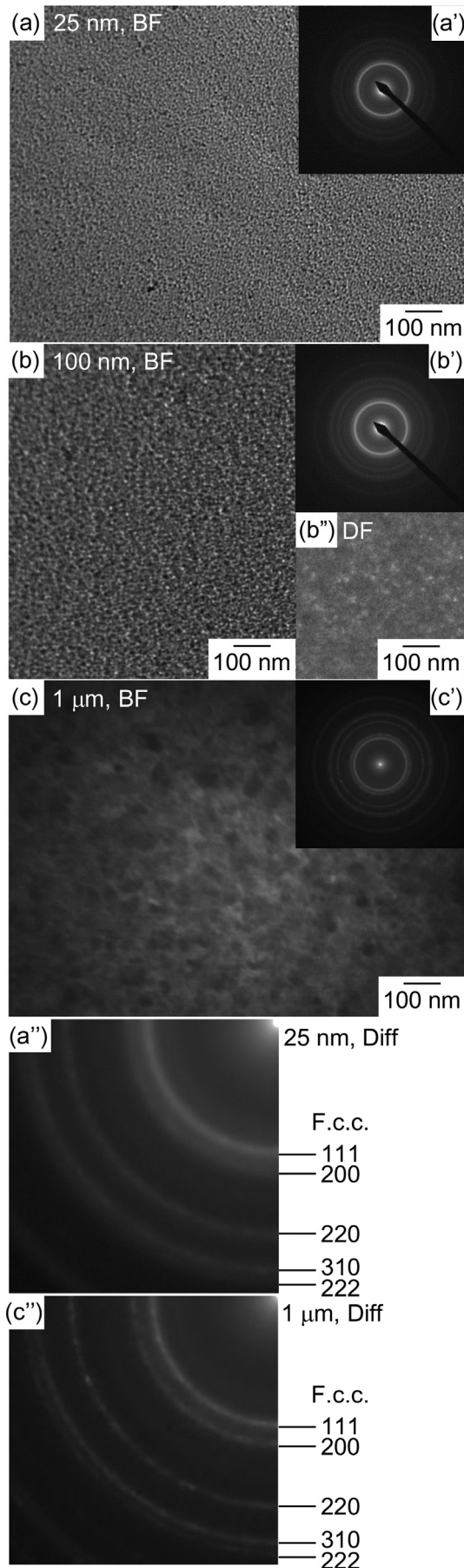


Fig. 3. HREM image and FFT pattern of the sputtered CoCrCuFeNi HEA specimens with a thickness of 25 nm.

the present study was a typical HEA with a single solid solution phase.

3.2. Structural changes induced by annealing

Fig. 4 shows *In situ* TEM images showing the annealing induced changes in the structure of 100 nm thick specimen induced by annealing of nano-crystalline CoCrCuFeNi HEA. The TEM specimen was heated under a pressure of about 8.0×10^{-6} Pa in the HVEM. The BF images acquired at 298 K (before annealing) and at 573 K did not exhibit any differences (Fig. 4(a)); however, the corresponding SAD patterns showed changes induced by annealing (Fig. 4(a')). With further annealing, grain coarsening of the crystalline phase was detected, and a typical example of a specimen heated to 998 K is shown in Fig. 4(b). The size of the grains present in the specimen annealed at 998 K was evaluated to be 48 nm by the intercept method of ASTM E112-60T. The SAD pattern acquired at 998 K (Fig. 4(b')) showed an alteration in the Debye rings. On heating, the continuous Debye rings changed to discontinuous rings and crystalline spots also appeared (Fig. 4(b')). To identify the structural changes of the 100 nm thick CoCrCuFeNi HEA caused by annealing, the electron diffraction intensity profiles were analyzed. The results of the analysis are shown in Fig. 5. In Fig. 5, the structure factors of the *fcc* and *bcc* solid solutions and the positions of the B2, L1₀, and L1₂ orderings are listed together with the intensity profiles. Before annealing (298 K), sharp intensity peaks corresponding to the *fcc* solid solution were observed. After heating to 573 K, new intensity profiles appeared. For instance, the intensity peak corresponding to the *bcc* phase (□), that corresponding to the B2 ordering (■), and the peak indicated by the letter A newly appeared. The diffraction intensity peak (A) will be discussed in section 4 in detail. Further annealing led to additional changes in the diffraction intensity profile. When the specimen was heated to 998 K, the peaks corresponding to B2 ordering disappeared. Some additional peaks (indicated by the letter X) were observed when the specimen was heated to 998 K. The phase which produces the X peaks cannot be identified, and is beyond the scope of the present study. From the

Fig. 2. TEM microstructures of sputtered specimens in CoCrCuFeNi high-entropy alloy (HEA) with various thickness. (a) (b) TEM-BF image, (a') (b') TEM-SAD pattern, (b'') TEM-DF image, (c) HVEM-BF image, (c') HVEM-SAD patterns, and (a'') (c'') phase identification of the crystalline phase based on the TEM-SAD and HVEM-SAD patterns. Specimen thicknesses are (a) (a') (a'') 25 nm, (b) (b') (b'') 100 nm, and (c) (c') (c'') 1 μm.

Table 1

The average (a) and standard deviation (b) of the alloy composition that were obtained by the analysis of 15 different positions in the same specimen, (c) ΔH_{mix} , ΔS_{mix} , and delta parameter.

Thickness [nm]	Co	Cr	Cu	Fe	Ni
(a) Average composition, at.%					
25	17.4	20.8	26.0	17.8	18.1
100	17.1	19.4	25.9	19.3	18.2
1000	17.0	18.5	26.9	18.8	18.8
(b) Standard deviation, at.%					
25	1.0	1.1	1.0	0.9	1.1
100	0.5	0.6	0.6	0.8	0.7
1000	0.7	0.3	0.5	0.7	0.4
(c) ΔH_{mix} [kJ/mol], ΔS_{mix} [kJ/mol K], Delta parameters					
Thickness [nm]	ΔH_{mix}	ΔS_{mix}	Delta		
25	13.3	13.3	2.5		
100	13.3	13.3	1.3		
1000	13.3	13.3	1.3		

tendency of the structural changes induced by annealing the nanocrystalline CoCrCuFeNi HEA samples, it can be noticed that (1) the *fcc* solid solution phase can remain as the main constituent phase during annealing up to 998 K, (2) a small amount of the *bcc* phase is formed through the *fcc-bcc* transition, (3) the appearance of the B2 ordering peak can be observed during annealing at

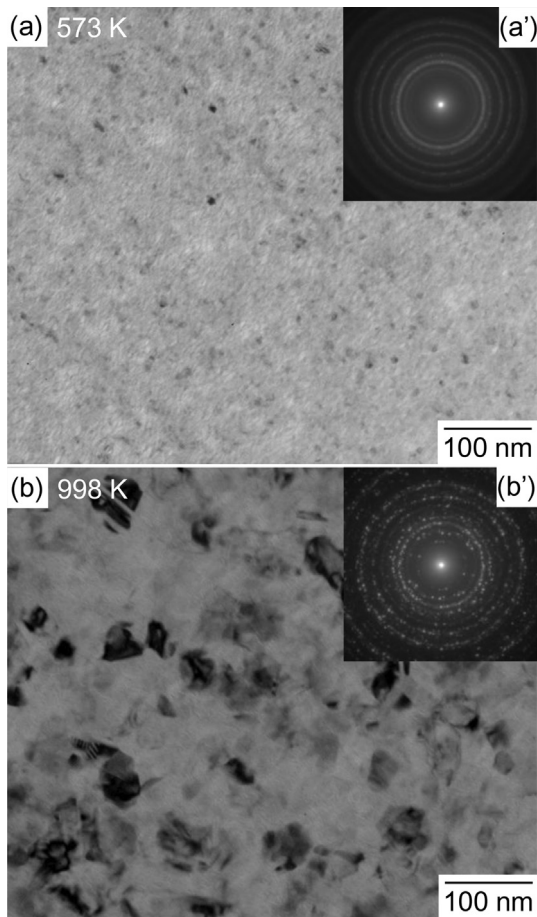


Fig. 4. *In-situ* TEM images showing the annealing induced changes in the structure of a 100 nm thick specimen of nanocrystalline CoCrCuFeNi HEA. The TEM specimen was heated under a vacuum exceeding 8.0×10^{-6} Pa in the HVEM to (a) 573 K and (b) 998 K.

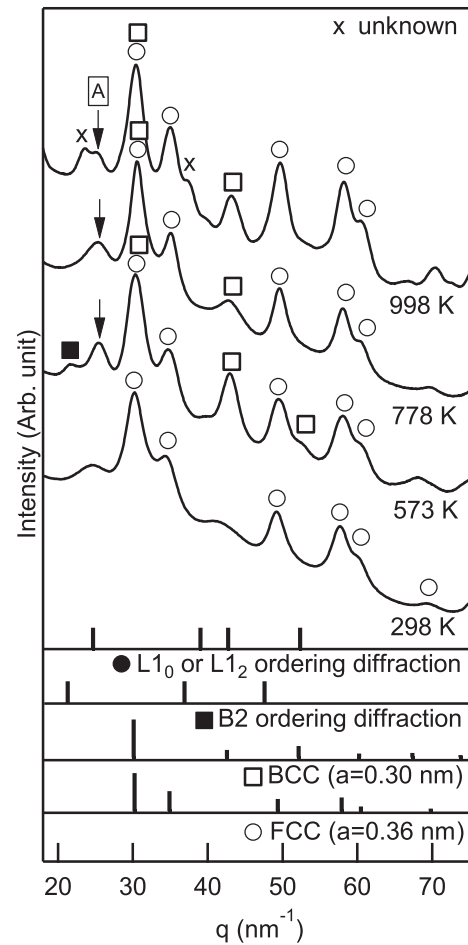


Fig. 5. Changes in the electron diffraction intensity profile of the 100 nm thick specimen of nanocrystalline CoCrCuFeNi HEA during *in situ* TEM annealing.

intermediate temperatures, and (4) grain coarsening occurs at around 998 K.

3.3. Structural changes induced by irradiation

Fig. 6 shows *in-situ* TEM images showing the changes in the structure of 100 nm thick specimen of nano-crystalline CoCrCuFeNi HEA induced by MeV electron irradiation at 298 K. The irradiation did not seem to lead to any changes in the sizes of the nanocrystalline grains, which is indicated by the BF images. This was the case despite of the heavy irradiation damage exceeding 60 dpa (Fig. 6(a)–(e)). In contrast, the SAD patterns indicated irradiation induced change. After 60 s of irradiation (Fig. 6(b') (b'')), the SAD pattern showed the appearance of new Debye rings indicated by the letter B. The intensity of the Debye ring B increased with increase in the irradiation dose, as shown in Fig. 6(c') (c'')–(e') (e''). The number of Debye rings showed the tendency to increase with the increase in the irradiation dose. To understand the irradiation induced changes observed in the SAD patterns, the electron diffraction intensity profile was analyzed and the results are shown in Fig. 7. The peak position of the intensity peak indicated by the letter A in Fig. 7 is similar to that indicated by the letter A in Fig. 5. The peaks indicated by the letter B in Fig. 7 correspond to those indicated by the letter B in the SAD patterns of Fig. 6. The *fcc* phase (○) remained as the main constituent phase after severe irradiation for 1.8×10^3 s. The peak indicated by the open square (□) appeared after 60 s of irradiation and the intensity increased with

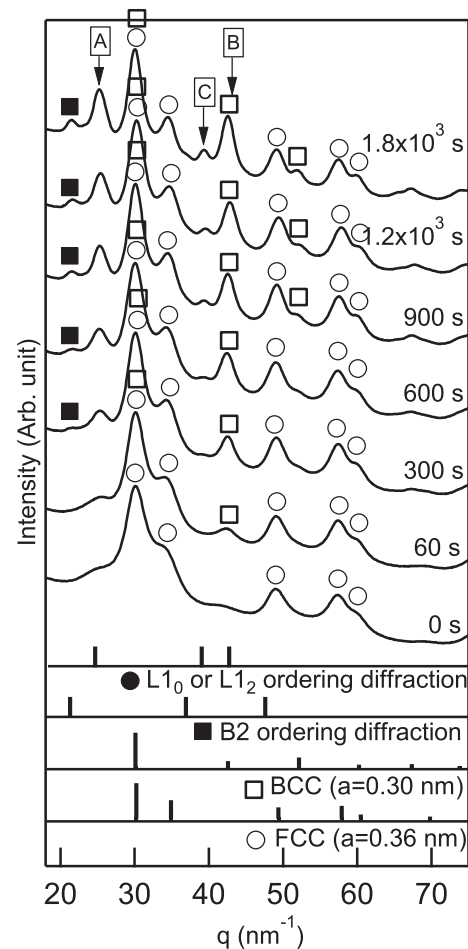
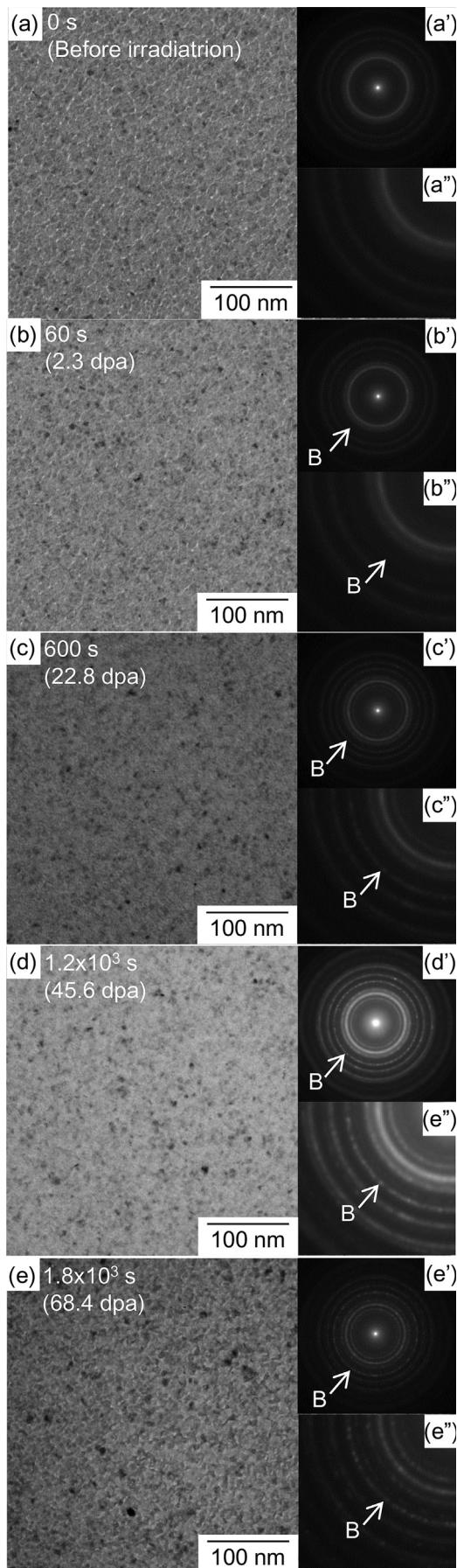


Fig. 7. Changes in electron diffraction intensity profile of the 100 nm thick specimen of nanocrystalline CoCrCuFeNi HEA caused by MeV electron irradiation at 298 K.

increase in the irradiation time. This indicates the *fcc* to *bcc* transition. The peak indicated by the filled square (■) appeared after irradiation for 300 s and these peaks are considered to correspond to the B2 ordering peak. The peaks indicated by the letters A and C also appeared after irradiation and the position of these peaks corresponds to the $L1_0$ and/or $L1_2$ orderings. These peaks (A and C) will be discussed in detail in section 4. The important findings obtained with regard to the structural changes induced by irradiation at 298 K can be summarized as follows. (1) The *fcc* solid solution phase remains as the main constituent phase, indicating that the *fcc* solid solution shows high phase stability against irradiation. (2) A small amount of *bcc* phase was formed through the *fcc* to *bcc* transition and the minor structural changes induced by irradiation is similar to that induced by the annealing. Also, (3) no grain coarsening was observed to occur as a result of the irradiation, while structural changes induced by annealing was accompanied by grain coarsening.

In general, structural changes in metallic materials induced by irradiation show significant temperature dependence. In the case of

Fig. 6. In-situ TEM images showing the changes in the structure of a 100 nm thick specimen of nanocrystalline CoCrCuFeNi HEA induced by MeV electron irradiation at 298 K a dose rate of $5.4 \times 10^{24} \text{ m}^{-2} \text{ s}^{-1}$ under a vacuum exceeding $8.0 \times 10^{-6} \text{ Pa}$. (a) (a') (a'') before irradiation, (b) (b') (b'') after irradiation for 60 s, (c) (c') (c'') after irradiation for 600 s, (d) (d') (d'') after irradiation for $1.2 \times 10^3 \text{ s}$, and (e) (e') (e'') after irradiation for $1.8 \times 10^3 \text{ s}$.

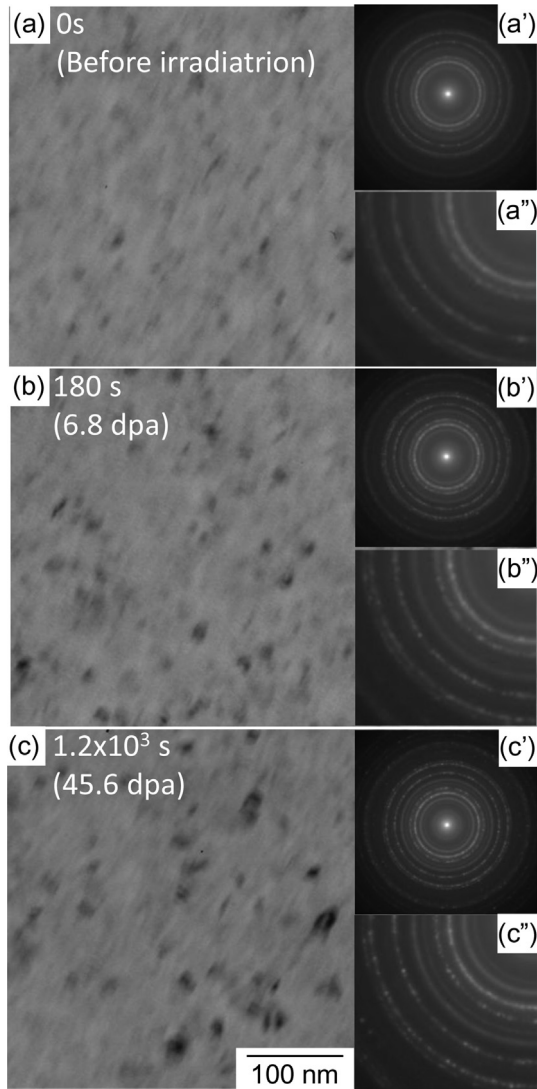


Fig. 8. In-situ TEM images showing the changes in the structure of a 100 nm thick specimen of nanocrystalline CoCrCuFeNi HEA induced by MeV electron irradiation at 773 K at a dose rate of $5.4 \times 10^{24} \text{ m}^{-2} \text{ s}^{-1}$ under a vacuum exceeding $8.0 \times 10^{-6} \text{ Pa}$. (a) (a') (a'') before irradiation, (b) (b') (b'') after irradiation for 180 s, (c) (c') (c'') after irradiation for $1.2 \times 10^3 \text{ s}$.

the multicomponent solid solution phase, the temperature dependence of structural changes induced by fast electron irradiation has been observed in Zr–Hf–Nb alloys [7,8]. In the present study, the temperature dependence of the phase stability of the *fcc* solid solution against fast electron irradiation was investigated by comparing the structural changes induced by irradiation at room temperature (Figs. 6 and 7) and that induced at 773 K (Figs. 8 and 9). Fig. 8 shows in-situ TEM images showing the changes in the structure of 100 nm thick specimen of nano-crystalline CoCrCuFeNi HEA induced by MeV electron irradiation at 773 K. The BF images (Fig. 8(a)–(c)) shows the nanocrystalline structure with a small amount of thermal drift effect. The grain coarsening by the irradiation cannot be seen in BF images at 773 K. In contrast, change in SAD patterns by the irradiation was observed. The SAD pattern after the irradiation at $1.2 \times 10^3 \text{ s}$ (Fig. 8(c')) seems to be similar to that at the specimen irradiated at 298 K for $1.2 \times 10^3 \text{ s}$ shown in Fig. 6(d') (d''), from the view points of the number and the position of Debye rings. Fig. 9 shows the changes in the electron diffraction

intensity profile of the 100 nm thick CoCrCuFeNi HEA specimen under fast electron irradiation at 773 K. Before irradiation, the main constituent phase was identified as the *fcc* solid solution phase and a minor phase of *bcc* solid solution, as already mentioned in Figs. 4 and 5, was present. The peaks indicated by the letters A, B, and C in Fig. 9 correspond to those shown in Figs. 5 and 7, respectively. The intensity of the peak indicated by the open square (\square), which corresponds to the *bcc* phase increased with the increase in the irradiation time. The peaks indicated by the filled square (\blacksquare) appeared after irradiation at 300 s, and these correspond to B2 ordering. The peaks A and C in Fig. 9 will also be discussed in the section 4 in detail. The irradiation-induced structural changes observed at 773 K (Figs. 8 and 9) are similar to those observed at 298 K (Figs. 6 and 7). The annealing induced structural change accompanied by the grain coarsening as shown in Figs. 4 and 5, while structural change without grain coarsening was introduced by the irradiation at 298 K and 773 K. The difference in grain coarsening behavior between thermal annealing and fast electron irradiation was not clarified now, and this may be explained by that in diffusion mechanism between thermal process and the irradiation enhanced mechanism. The characteristics of the phase stability of the multicomponent *fcc* solid solution in CoCrCuFeNi HEA against irradiation at 773 K can be summarized as follows. (1) The *fcc* solid solution shows high phase stability against irradiation at 773 K as well as at 298 K. (2) A small amount of minor phases may appear at 773 K and this behavior is similar to the structural changes induced by thermal annealing and those induced by irradiation at 298 K. (3)

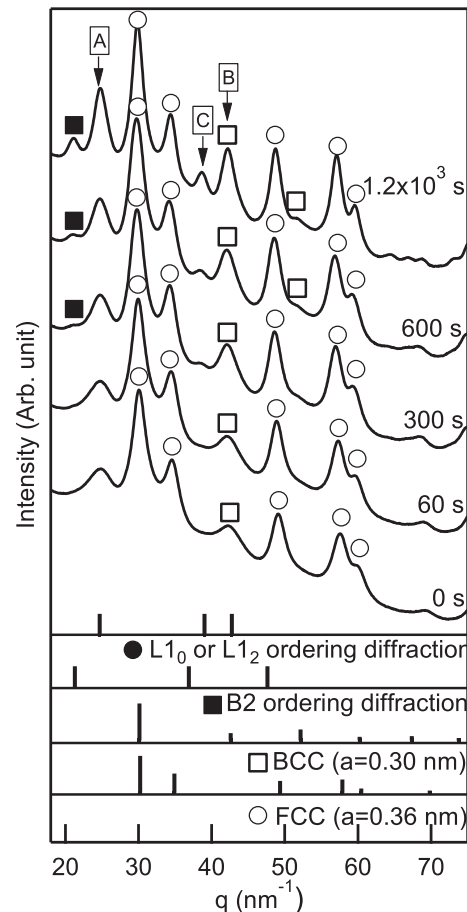


Fig. 9. Changes in the electron diffraction intensity profile of a 100 nm thick specimen of nanocrystalline CoCrCuFeNi HEA caused by MeV electron irradiation at 773 K.

Grain coarsening of the fine grained *fcc* solid solution hardly occurred under irradiation at and below 773 K.

4. Discussion

4.1. Phase stability of the *fcc* solid solution phase against irradiation

Our experimental results clearly demonstrate that the *fcc* solid solution in CoCrCuFeNi HEA shows high phase stability against heavy irradiation damage over 60 dpa at 298 K and 40 dpa at 773 K. A small amount of the *bcc* solid solution phase appears because of the irradiation; however, the *fcc* solid solution remains as the main constituent phase. The characteristics of the irradiation-induced structural changes observed in the present study were similar to the annealing-induced structural changes, specifically in view of the changes in constituent phases. However, grain coarsening observed during thermal annealing could not be observed during irradiation. The present study is the first demonstration of the significantly high phase stability of a five-component HEA against fast electron irradiation.

Fig. 10 shows the schematic illustrations of the simplest type of defects introduced by the electron knock-on effect under MeV electron irradiation, and the defect recovery processes in single

element solid solutions as a typical example of conventional metallic materials (a) (a') and these in HEA (b) (b') (b''). Under MeV electron irradiation, in the case of a single component solid solution, an interstitial (I) and a vacancy (V), i.e., a Frenkel pair, were formed through a single atom displacement by the electron knock-on effect (Fig. 10(a)). A simple model for the evolution of I and V is shown in Fig. 10(a'). The introduction of I and V leads to irradiation damages, such as an accumulation of dislocation loops (I-type, ③+④) (V-type, ⑤+⑥), formation of voids (⑤+⑥), etc. The atomic diffusion of constituent elements was enhanced by the migration of I and V (②), I–V recombination (①), and by the annihilation of I and V at sinks such as grain boundaries (⑦). In the case of HEAs subjected to MeV electron irradiation, unique factors, which can be ignored in conventional metallic materials, must be considered with regard to the defect recovery processes. As shown in Fig. 10(b) (b'), a large variety of Is and Vs are produced in HEAs. Some Is and Vs may show significantly high formation energies and/or low migration energies, resulting in high atomic-level stress and/or anomalously high migration of Is and Vs. The high atomic-level stress in HEAs may facilitate amorphization upon irradiation (⑩ in Fig. 10(b'')), followed by recrystallization (⑪ in Fig. 10(b'')). Hence, this process is expected to leave much less defects in HEAs than in conventional materials [5]. The amorphization–recrystallization

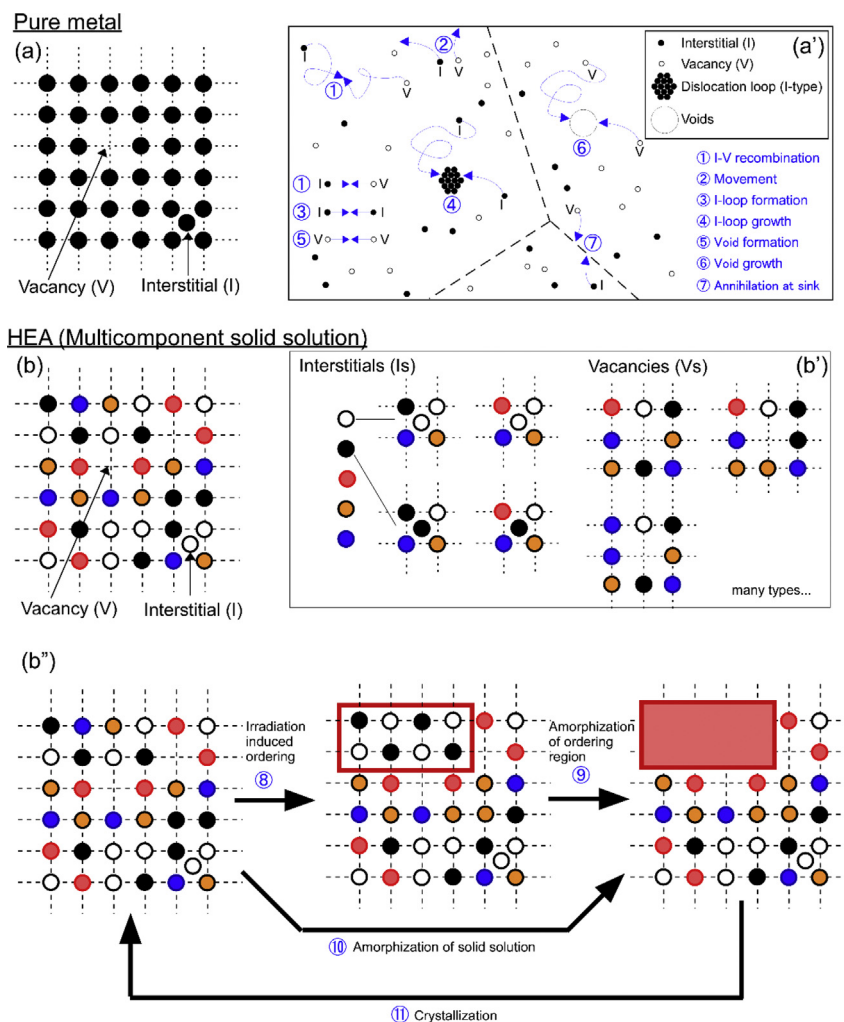


Fig. 10. Schematic illustration of the simplest type of defects introduced by the electron knock-on effect under MeV electron irradiation and defect recovery processes. (a) (a') single component crystal, namely, the pure metal, (b) (b') (b'') multicomponent solid solution in HEAs. (b'') is the schematic illustration of the defect recovery via amorphization–recrystallization process.

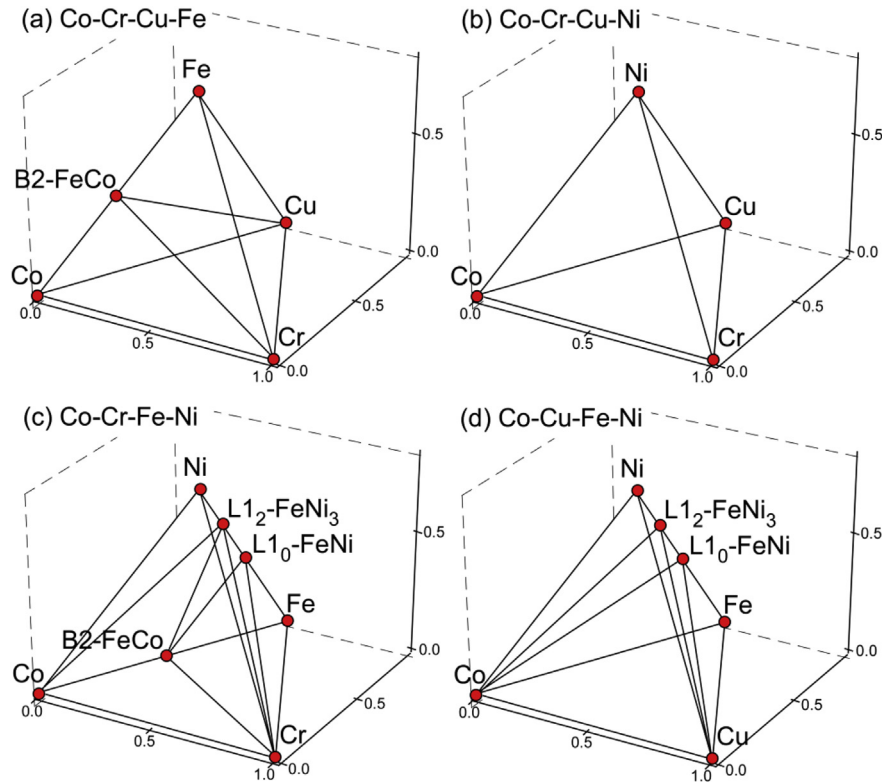


Fig. 11. The combination of quaternary phase diagrams of the five-component CoCrCuFeNi HEA reported in Materials Projects.

process occurring under the irradiation has been reported in some binary and ternary alloy systems in which amorphization is followed by crystallization [17] and a crystal-to-amorphous-to-crystal (C–A–C) transition in intermetallic compounds occurs [18–20]. The experimental reports of C–A–C implies that the occurrence of irradiation damage healing in Fig. 10(b'') may be possible in HEAs. The abovementioned type of phase transitions, namely, amorphization–recrystallization process (⑩ and ⑪) and/or C–A–C transition after the irradiation induced ordering (⑧, ⑨ and ⑪), were not clarified in detail because of the absence of systematic studies on the irradiation damage evaluation in HEAs. The experimental results of this study (i.e., the extremely high phase stability of the *fcc* solid solution against irradiation) may also be indicative of the occurrence of a unique damage recovery process (Fig. 10(b) (b') (b'')) for realizing the high phase stability of a solid solution phase. It is to be noted that the annihilation of Is and Vs at the grain boundaries (⑦) exerts a major impact on the irradiation-enhanced diffusion and damage annihilation in nanocrystalline materials. To clarify the differences between the defect recovery processes occurring in conventional solid solution phases (Fig. 10(a) (a')) and HEAs (Fig. 10(b) (b') (b'')), experimental data need to be acquired from the HEA specimens with coarse crystalline grains. However, we can emphasize here that the *in-situ* TEM observations carried out in the present study on the irradiation damage evolution process in HEAs is a direct experimental evidence of the high phase stability of this material against irradiation damage. The results of the experimental study focusing on the damage evolution process in HEAs with coarse crystalline grains by HVEM, and *in-situ* HREM observation for clarifying the damage recovery process via amorphization and crystallization shown in Fig. 10(b''), will be reported in future papers, which will help enable the development of a new generation of structural materials with superior resistance to irradiation damage.

In the present study, minor irradiation-induced structural change, which is similar to that induced by thermal annealing, has been observed, while grain coarsening was not observed under irradiation. As shown in Fig. 10, irradiation-enhanced diffusion mechanism is different from thermal diffusion. This may lead to the differences observed in grain coarsening during annealing and irradiation.

4.2. The formation of an ordered phase and precipitation of intermetallic compounds under fast electron irradiation

The formation of an ordered phase and the precipitation of intermetallic compounds in HEAs are important problems because these phenomena affect the mechanical properties and the change in volume of the irradiated materials. Furthermore, the irradiation induced ordering (⑧ in Fig. 10(b'')) may be effective to stimulate the unique damage recovery process via amorphization and crystallization in HEAs. A database of thermal equilibrium phase diagrams and of the experimental results about MeV electron irradiation induced structural changes can offer useful information. In this section, we suggest the idea of evaluating the possibility of the formation of an ordered phase and precipitation of intermetallic compounds under irradiation. Fig. 11 shows the combination of quaternary phase diagrams in CoCrCuFeNi HEA constructed by Materials Projects based on first principles calculations [21–24]. The existence of *bcc*-based B2–FeCo, *fcc*-based L1₂–FeNi₃, and L1₀–FeNi can be seen in Co–Cr–Cu–Fe (a), Co–Cr–Fe–Ni (c), and Co–Cu–Fe–Ni (d) alloys systems, where the formation energy of each ordered phases was 5.8 kJ/mol, 8.5 kJ/mol, and 6.7 kJ/mol, respectively. Table 2 summarizes the intermetallic compounds and the *bcc* and *fcc*-based ordered phases reported in the binary phase diagrams of Co–Cr [25], Co–Cu [26], Co–Fe [27], Co–Ni [28,29], Cr–Cu [30,31], Cr–Fe [32], Cr–Ni [33,34], Cu–Fe [35,36], Cu–Ni

Table 2
Formation of (a) intermetallic compounds with complex structures, (b) *bcc*-based B2 phase, (c) *fcc*-based L1₀ phase, and (d) *fcc*-based L1₂ phase, as reported in the phase diagram of various binary alloy systems formed from Co, Cr, Cu, Fe, and Ni.

(a) intermetallics with complex structures					
	Co	Cr	Cu	Fe	Ni
Co		σ-phase			
Cr				σ-phase	
Cu					
Fe					
Ni					
(b) <i>bcc</i> -based B2 phase					
	Co	Cr	Cu	Fe	Ni
Co				CoFe (995 K)	
Cr					
Cu					
Fe					
Ni					
(c) <i>fcc</i> -based L1 ₀ phase					
	Co	Cr	Cu	Fe	Ni
Co					
Cr					
Cu					
Fe					FeNi (728 K)
Ni					
(d) <i>fcc</i> -based L1 ₂ phase					
	Co	Cr	Cu	Fe	Ni
Co					
Cr					
Cu					
Fe					FeNi ₃ (~ 773 K)
Ni					

[37], and Fe–Ni [38–40] alloy systems, along with the ordering temperature. Based on this dataset, we can focus on compounds and/or ordered phases, which have a possibility to appear under irradiation. It is sufficient to consider the formation of the *bcc*-based B2–FeCo phase, *fcc*-based L1₂–FeNi₃ and L1₀–FeNi phases, and σ–CrFe and CoCr phases under MeV electron irradiation in CoCrCuFeNi HEA.

It is well-known that various intermetallic compounds and ordered phases transform to a disordered solid solution and/or an amorphous phase under MeV electron irradiation. These phases with low phase stability against irradiation cannot appear from multicomponent solid solution phases under irradiation. The experimental database of the irradiation-induced structural changes in intermetallic compounds focusing on the occurrence of amorphization (over 80 compounds) has been constructed by research center for ultra-high voltage electron microscopy in Osaka University [16,41] (see Table 3). The possibility of the occurrence of irradiation-induced ordering and the precipitation of intermetallic compounds can be predicted by using a systematically constructed database. In Table 3, only the possibility of σ–CrFe can be noted, where the amorphization of σ–CrFe was not observed. The

irradiation-induced structural change in σ–CrFe has been investigated by Anada et al. in detail and it is known that this phase changes to a *bcc* solid solution phase under MeV electron irradiation at and above 298 K [42]. This result indicates that irradiation cannot enhance σ–CrFe formation and this prediction seemed to be in good agreement with the experimental results presented here. The appearance of a weak diffraction peak corresponding to B2 ordering can be detected during annealing and under irradiation at 298 K (Fig. 7) and 773 K (Fig. 9) of the CoCrCuFeNi HEA specimens. Fig. 10 and Table 2(b) show the B2 structure formation only in the Fe–Co alloy system among the combinations of Co, Cr, Cu, Fe, and Ni. The possibility of B2 ordering occurring in the case of Fe–Co based systems can be considered to be higher than that with other pairs. The irradiation-induced amorphization of B2 compounds has been systematically investigated and reported previously [43,44]; B2 compounds which show martensite transition (such as B2–ZrCu, B2–TiNi, and B2–Ti(Ni, Fe)) have been demonstrated to show a tendency to exhibit solid state amorphization. In contrast, other compounds (such as NiAl) can maintain the crystalline structure under irradiation. The experimental data of the irradiation-induced structural changes in B2–FeCo, which does not

Table 3

The experimental database of the occurrence of solid-state amorphization (crystal to amorphous transition) in intermetallic compounds under MeV electron irradiation.

Compounds	Experiment	Compounds	Experiment
Al ₂ Au	No	BNi	No
Al ₂ Cu	No	B ₃ Ni ₄ (m)	No
AlCu(η ²)	No	BNi ₃	No
Al ₉ Co ₂	Yes	Co ₃ Ti	No
Al ₅ Co ₂	No	Co ₂ Ti	Yes
Al ₇ Cr	Yes	CoTi	No
Al ₅ Cr	Yes	CrFe	No
Al ₄ Cr	Yes	Cr ₂ Zr	Yes
Al ₉ Cr ₄	No	Cr ₂ Ti	Yes
Al ₈ Cr ₅	No	Cu ₃ Ti ₂	Yes
AlCr ₂	No	Cu ₄ Ti ₃	Yes
Al ₃ Fe	Yes	CuTi	Yes
Al ₅ Fe ₂	No	CuTi ₂	Yes
Al ₂ Fe	No	Cu ₄ Ti	No
AlFe	No	CuPt ₇	No
Al ₆ Mn	Yes	Cu ₁₀ Zr ₇	Yes
Al ₄ Mn	Yes	CuZr	Yes
Al ₃ Mn	No	CuZr ₂	Yes
Al ₁₁ Mn ₄	No	Fe ₁₇ Nd ₂	Yes
AlMn (γ ²)	No	Fe ₂ Ti	Yes
Al ₁₂ Mo	No	FeTi	No
Al ₈ Mo ₃	No	FeZr ₂	Yes
Al ₃ Ni	No	FeZr ₃	Yes
Al ₃ Ni ₂	No	Mn ₂ Ti	Yes
AlNi	No	MoNi	Yes
AlNi ₃	No	Nb ₇ Ni ₆	Yes
Al ₁₀ V	Yes	NbNi ₃	No
Al ₄₅ V ₇	Yes	NiTi	Yes
Al ₂₃ V ₄	Yes	NiTi ₂	Yes
Al ₃ V	No	Ni ₃ Ti	No
Al ₈ V ₅	No	Ni ₃ Zr	Yes
Al ₃ Ti	No	NiZr	Yes
Al ₂ Zr	Yes	NiZr ₂	Yes
Al ₃ Zr ₂	Yes	PdTi ₂	No*
AlZr	Yes	PdZr ₂	Yes
Al ₄ Zr ₅	Yes	Pt ₃ Zr ₅	Yes
Al ₃ Zr ₄	Yes	Fe ₂₃ Nd ₂ B ₃	Yes
Al ₂ Zr ₃	Yes	Fe ₁₄ Nd ₂ B	Yes
AlZr ₂	Yes	Fe ₈₁ Zr ₉ B ₁₀	Yes
Al ₃ Zr	No	Fe ₄ Nd _{1,1} B ₄	No
AlZr ₃	No	Ti ₅₀ Ni ₄₈ Fe ₂	Yes
Al ₁₂ W	No	Ti ₅₀ Ni ₄₄ Fe ₆	Yes
BCo ₂	Yes	Ti ₅₀ Ni ₄₀ Fe ₁₀	Yes
BCo ₃	Yes	Ti ₅₀ Ni ₃₀ Fe ₂₀	Yes
BCo	No	Ti ₅₀ Ni ₂₀ Fe ₃₀	Yes
BFe ₃	Yes	Ti ₅₀ Ni ₁₀ Fe ₄₀	Yes
BFe ₂	No		
B ₃ Ni ₄ (o)	Yes		
BNi ₂	Yes		

Note: This list was first developed by H. Mori [41] and most of the data has been acquired from this list (which was updated on 4/February/2014).

No*: partial amorphization.

Table 4

The experimental database of the occurrence of irradiation induced ordering under MeV electron irradiation.

Compounds	Experiment	Ref.
AlNi ₃	No	[45]
AlZr ₃	No	[47,48]
AuCu ₃	Yes*	[49,50]
CuPt ₇	Yes	[51]
CuZn	Yes*	[52]
FeNi	Yes	[46]
Ni ₄ Mo	Yes	[53,54]
Ni ₃ Mn	Yes*	[55]

Yes*: irradiation and post-irradiation annealing.

This list was first developed by E.M. Schulson [45], and has been modified in the present study (which was updated on 22/November/2014).

show the martensite phase transition, has not been reported (Table 3); however, the systematic study conducted on MeV electron irradiation-induced amorphization in B2 compounds implies that the possibility of the occurrence of Fe–Co-related B2 ordering under MeV electron irradiation is higher than that for other systems.

Ordering behavior induced by MeV electron irradiation has been reported in various alloy systems and summarized in a review paper [45]. Table 4 shows the list of compounds which have been studied for irradiation-induced ordering and disordering in the literature [45], together with recent experimental data. Among FeCo, Fe₃Ni, FeNi, CrFe, and CoCr, the occurrence of irradiation induced ordering of L1₀–FeNi from disordered Fe–Ni alloy (Fe_{69.1}Ni_{30.9}–Fe_{51.2}Ni_{48.8} at.%) under 1 MeV electron irradiation at a temperature below 593 K [46] has been reported. The electron diffraction intensity peaks indicated by the letter A in the case of the annealed specimen (Fig. 5), those indicated by the letters A, B, and C in the case of the specimen irradiated at 298 K (Fig. 7), and those indicated by the letters A, B, and C in the case of the specimen irradiated at 773 K (Fig. 9) correspond to the ordering diffractions of L1₀ and/or L1₂. The electron irradiation-induced ordering of L1₀–FeNi reported by Reuter et al. [46] implies the possibility of the occurrence of L1₀ ordering in Fe–Ni related alloys at 298 K under MeV electron irradiation. The occurrence of irradiation-induced L1₀ ordering in Fe–Ni related alloys at 773 K is still unclear. The presence of Co, Cu, and/or Cr elements may increase the ordering temperature of Fe–Ni-related L1₀ structures in the CoCrCuFeNi HEA. We only speculate this, and the experimental results are insufficient to discuss this phenomenon. Hence, further experimental data are required to conclude the occurrence of irradiation-induced ordering and precipitation of compounds in the CoCrCuFeNi HEA. However, it should be emphasized that the combination of the phase diagrams predicted based on first principle calculation (Fig. 11), the reported binary phase diagrams (Table 2), the experimental database of the irradiation-induced solid state amorphization (SSA) in compounds under MeV electron irradiation (Table 3) [16,41], and irradiation-induced ordering (Table 4) [45] offers useful information about the possibility of the occurrence of irradiation-induced ordering and/or precipitation of compounds in multicomponent HEAs.

To note, the intensity of peak A observed in the case of the annealed specimen is much lower than that observed in the case of irradiated specimens and the peak B observed in the case of the irradiated specimens overlapped with the bcc peak. The occurrence of fcc-based ordering during annealing is difficult to confirm because only one peak with a low intensity was observed.

5. Conclusions

In the present study, we investigated the irradiation-induced structural changes and phase stability for multicomponent CoCuCrFeNi HEAs under fast electron irradiation by HVEM. Based on the results of our study, the following conclusions can be drawn:

- (1) The *fcc* solid solution shows high phase stability against irradiation and the *fcc* phase remained as the main constituent phase over 40 dpa of irradiation at 298 K and 773 K. This is the first study to provide experimental evidence for high phase stability in a five-component HEA against irradiation.
- (2) The irradiation produces minor structural changes, which are similar to the structural changes induced by thermal annealing in HEA (i.e. *fcc* to *bcc* phase transition), while grain coarsening was not observed under irradiation.
- (3) We also suggest a method for predicting the irradiation-induced ordering and/or the formation of compounds in

HEAs under irradiation. The combination of the predicted phase diagram obtained based on the first principles calculations, the reported binary phase diagrams, the experimental database of the irradiation-induced amorphization in compounds under MeV electron irradiation, and irradiation induced ordering offers useful information about the possibility of the occurrence of irradiation-induced ordering and the precipitation of compounds in multicomponent HEAs.

Acknowledgments

This work was supported in part by the Grants for Excellent Graduate Schools from the Ministry of Education, Culture, Sports, Science, and Technology, Japan. PDR and JHN acknowledge support from the Joint Institute for Advanced Materials at the University of Tennessee and the Oak Ridge National Laboratory. TE acknowledges support from the Department of Energy through the NEUP program, DE-AC07-05ID14517.

References

- [1] Ranganathan S. *Curr Sci* 2003;85:1404.
- [2] Cantor B, Chang ITH, Night PK, Vincent AJ. *Mater Sci Eng A* 2004;375:213.
- [3] Yeh JW, Chen SK, Lin SJ, Gan JY, Chin TS, Shun TT, et al. *Adv Eng Mater* 2004;6:299.
- [4] Zhang Y, Zhou YJ, Lin JP, Chen GL, Liew PK. *Adv Eng Mater* 2008;10:534.
- [5] Egami T, Guo W, Rack PD, Nagase T. *Metall Mater Trans A* 2014;45:180.
- [6] Nagase T, Anada S, Rack PD, Noh JH, Yasuda H, Mori H, et al. *Intermetallics* 2012;26:122.
- [7] Nagase T, Anada S, Rack PD, Noh JH, Yasuda H, Mori H, et al. *Intermetallics* 2013;38:70.
- [8] Rar A, Frafjord JJ, Fowlkes JD, Specht ED, Rack PD, Santella ML, et al. *Meas Sci Technol* 2005;16:46.
- [9] Kiritani M, Yoshida K, Fujita H. *Proc fifth int conf on high voltage electron microscopy*. 1977. p. 501. Tokyo.
- [10] Mckinley WA, Feshbach H. *Phys Rev* 1948;74:1759.
- [11] Corbett JW. *Electron radiation damage in semiconductors and metals*. New York: Academic Press; 1966.
- [12] Oen OS. *Nucl Inst Meth Phys Res B* 1988;33:744.
- [13] Urban K. *Phys Stat Sol A* 1979;56:157.
- [14] Urban K. *Electron Microsc* 1980;4:188.
- [15] Nagase T, Sando T, Nino A, Qin W, Yasuda H, Mori H, et al. *J Non Cryst Solids* 2012;358:502.
- [16] Nagase T. *Advanced materials design by irradiation of high energy particles*. In: Kakeshita T, editor. *Progress in advanced structural and functional materials design*. Springer; 2013. p. 137.
- [17] Sinkler W, Luzzi DE, Allen CW. *Scr Metall* 1993;28:863.
- [18] Nagase T, Umakoshi Y. *Scr Mater* 2003;48:1237.
- [19] Nagase T, Nino A, Hosokawa T, Umakoshi Y. *Mater Trans* 2007;48:1651.
- [20] Anada S, Nagase T, Yasuda H, Mori H. *J Alloys Compd* 2013;579:646.
- [21] Jain A, Hautier G, Moore C, Ong SP, Fischer C, Mueller T, et al. *Comp Mater Sci* 2011;50:2295.
- [22] Ong SP, Jain A, Hautier G, Kocher M, Cholia S, Gunter D, et al. *The Materials Project*. <http://materialsproject.org> [accessed on 30.05.14].
- [23] Ong SP, Wang L, Kang B, Ceder G. *Chem Mater* 2008;20:1798.
- [24] Jain A, Hautier G, Ong SP, Moore C, Fischer C, Persson K, et al. *Phys Rev B* 2011;84. 045115–1.
- [25] Okamoto H. *J Phase Equilib* 2003;24:377.
- [26] Palumbo M, Curiotto S, Battezzati L. *Calphad* 2006;30:171.
- [27] Ustinovshikov YI, Pushkarev BE, Sapegina IV. *Inorg Mater* 2006;42:354.
- [28] Haschimoto U. *Nippon Kinzoku Gakkaishi* 1937;1:177 [in Japanese].
- [29] Nishizawa T, Ishida K. In: Massalski TB, editor. *Binary alloy phase diagrams*. 2nd ed., vol. 2; 1990.
- [30] Leonov MP, Bochvar NR, Ivanchenko VG. *Phys Chem* 1986;290:886.
- [31] Chakrabarti DJ, Laughlin DE. In: Massalski TB, editor. *Binary alloy phase diagrams*. 2nd ed., vol. 2; 1990.
- [32] Chen SL, Zhang JY, Lu XG, Chou K, Chang YA. *J Phase Equilib Diffus* 2006;27:121.
- [33] Okamoto H. *J Phase Equilib* 1997;18:221.
- [34] Turchi PEA, Kaufman L, Liu ZK. *Calphad* 2006;30:70.
- [35] Amara SE, Belhadj A, Kesri R, Hamar Thibault S. *Z Met* 1999;90:116.
- [36] Bein S, Colinet C, Durand Charre M. *J Alloys Compd* 2000;313:133.
- [37] Miettinen J. *Calphad* 2005;29:40.
- [38] Tomiska J, Neckel A. *Ber Bunsen Ges*. 1985;89:1104–9.
- [39] Reuter KB, Williams DB, Goldstein JL. *Metall Trans A* 1989;20:719.
- [40] Yang CW, Williams DB, Goldstein JL. *J Phase Equilib* 1996;17:522.
- [41] Mori H. *Current topics in amorphous materials*. In: Sakurai Y, Hamakawa Y, Masumoto T, Shirae K, Suzuki K, editors. *Physics and technology*. Amsterdam: Elsevier Science Publishers; 1997. p. 120–6.
- [42] Anada S, Nagase T, Kobayashi K, Yasuda H, Mori H. *Acta Mater* 2014;71:195.
- [43] Nagase T, Sasaki A, Yasuda HY, Mori H, Terai T, Kakeshita T. *Intermetallics* 2011;19:1313.
- [44] Nagase T, Sasaki A, Takizawa K, Yasuda HY, Terai T, Fukuda T, et al. *J Soc Mater Sci – Jpn* 2013;62:185 [in Japanese].
- [45] Schulson EM. *J Nucl Mater* 1979;83:239.
- [46] Reuter KB, Williams DB, Goldstein JL. *Metall Trans A* 1989;20:711.
- [47] Carpenter GJC, Schulson EM. *J Nucl Mater* 1978;23:180.
- [48] Howe LM, Rainville M, Schulson EM. *J Nucl Mater* 1974;50:139.
- [49] Adam J, Green A, Dugdab RA. *Phil Mag* 1952;43:1216.
- [50] Dixon CE, Meechan CJ, Brinkman JA. *Phil Mag* 1953;44:449.
- [51] Nagase T, Seno Y, Yasuda H, Mori H. unpublished work.
- [52] Koczak MJ, Herman H, Damask AC. *Acta Met* 1971;19:303.
- [53] Banerjee S, Urban K. *Phys Stat Sol* 1984;81:145.
- [54] Banerjee S, Urban K, Wilkens M. *Acta Metall* 1984;32:299.
- [55] Decker D, Dworschak F, Lehmann C, Rie KT, Schuster H, Wollenberger H, et al. *Phys Stat Sol* 1968;30:219.